IEEE Access
Multidisciplinary | Rapid Review | Open Access Journal

Received 19 September 2024, accepted 16 November 2024, date of publication 26 November 2024,
date of current version 17 December 2024.

Digital Object Identifier 10.1109/ACCESS.2024.3506722

RESEARCH ARTICLE

D-Band Scalable Phased Array Antenna-in-Package Using Stripline Power Divider-Based Sub-Array

HYUNJIN KIM, (Member, IEEE), AND JUNGSUEK OH, (Senior Member, IEEE)
Department of Electrical and Computer Engineering, Institute of New Media and Communications (INMC), Seoul National University, Seoul 08826, South Korea

Corresponding author: Jungsuek Oh (jungsuek@snu.ac.kr)

This work was supported in part by the Institute of Information and Communications Technology Planning and Evaluation (IITP) Grant funded by Korea Government (MSIT), Development of Key Technologies for 6G RF Front-End Based on Low-Power MIMO and Highly Efficient Spatial QAM Synthesis, 50%, under Grant 2021-0-00198; and in part by the Basic Science Research Program through the National Research Foundation of Korea (NRF) funded by the Ministry of Education under Grant 2022R1A6A3A01085999.

ABSTRACT This article presents an overview and recent design for the sub-array antenna-in-package (AiP) structures of scalable phased array for D-band applications. The primary focus is on the benefits and challenges associated with the design of scalable phased arrays at D-band frequencies. Following this, a sub-array structure of stripline power divider (PD)-based AiP is proposed. Initially, an analysis of a dual-polarized antenna element is conducted, employing characteristic modes and equivalent circuits. Subsequently, two distinct PDs are developed to match the antenna elements for sub-array setups. These configurations achieved notable results, including a 42.8% impedance bandwidth, port-to-port isolation exceeding 15 dB, and a 3 dB gain bandwidth exceeding 43%. Furthermore, a 4×4 antenna array is designed that attained notable specifications, such as a maximum gain of 16.7 dBi, a radiation efficiency of 80.7%, and a cross-polarization discrimination (XPD) of over 20 dB at 140 GHz. To validate these accomplishments, a measurement setup was established that could be vertically mounted incorporating bulky frequency extension units and waveguides. This setup successfully confirmed the extensive bandwidths and radiation patterns of the 4×4 antenna array.

INDEX TERMS 6G, D-band, multilayer PCB, antenna-in-package, sub-array.

I. INTRODUCTION

Currently the D-band frequency band (ranging from 110 GHz to 170 GHz) has received increasing attention for its applications in imaging, satellite, radar applications, and sixth generation (6G) communication systems [1], [2]. In particular, 6G communication is expected to allocate a wide bandwidth to provide enhanced data rates. The D-band can provide a considerable amount of available bandwidth, which satisfies the 6G requirement for the Tbps data rate. Moreover, the Federal Communications Commission opened the spectrum between 95 GHz and 3,000 GHz for experimental use and unlicensed applications to accelerate the development of future wireless communication technologies [3]. Consequently, mobile communications will be expected to utilize D-bands in the next wireless system.

However, for the realization of D-band communication, several challenges must first be addressed, one of which is the free-space path loss, which is proportional to the square of the frequency, following Friis' equation. For example, the path loss at 140 GHz is approximately 14 dB higher than that at 28 GHz. Additionally, the effect of atmospheric absorption in the D-band is typically more severe than that at lower frequencies because of the absorption of oxygen and water [4]. Hence, massive antenna arrays are required to compensate for these losses. Realizing such arrays that operate at D-band frequencies poses another challenge in designing antenna elements and feeding networks to

The associate editor coordinating the review of this manuscript and approving it for publication was Bilal Khawaja.

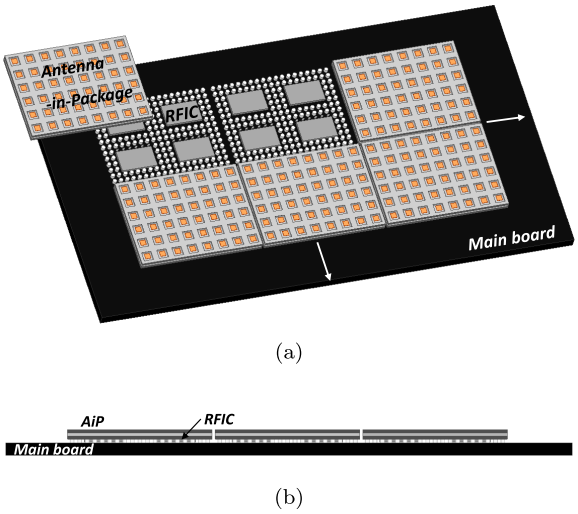

FIGURE 1. (a) Concept and configuration of the scalable phased arrays based on AiP at 140 GHz; (b) Side view of the concept.

achieve wide bandwidth. Moreover, the use of massive antenna arrays results in very sharp beams. Thus, the beam-forming architecture must be optimized to provide fast beam scanning and wide coverage at a reasonable cost and energy consumption.

Applying massive phased arrays with an N_T-antenna array and N_T-array transmitter (Tx) of radio frequency integrated circuits (RFIC) results in N_T^2 improvement in the effective isotropic radiated power (EIRP). For an N_T^2 increase in the EIRP, the phased array consumes only N_T times the power because N_T times higher power is focused on a radiation pattern with an N_T times smaller beam width. In a phased-array receiver (Rx), the signal-to-noise ratio (SNR) improves with N_R. The signal power increases by a factor of N_R^2 and the total noise power by a factor of N_R [5]. The general architecture for implementing massive phased arrays is commonly known as a scalable phased array, which involves the integration of repeatable antennas and RFIC units [6]. A popular configuration for Si-based scalable phased arrays is illustrated in Fig. 1 [7], [8].

As shown in Fig. 1, four RFICs are combined within a single AiP, and there are four channels in one TRx RFIC. Each RFIC channel could be required to cover three or four antenna elements. To address this issue, the subarray concept can be introduced, which will be discussed in Section II. The subarray antenna can be realized using the microstrip line, stripline, and substrate integrated waveguide (SIW). A series-fed microstrip patch antenna array is widely used in various studies, particularly in frequency-modulated continuous wave (FMCW) radar systems [9], [10], [11], [12]. The series-fed array structure employs a shorter line, which results in an antenna with less space on the substrate and lower attenuation loss [13]. Additionally, microstrip technology can provide a shaped beam that can be synthesized with patch antennas of different lengths and widths. Moreover, the microstrip-line-based design offers design flexibility because varying the impedance of the microstrip feed lines is easy. However, patch antenna design is based on an inset-feed structure, and the bandwidth is limited compared with other design approaches, such as the stripline and SIW.

Several stripline-fed antenna arrays are used for backhauling, power detectors, and FMCW radar applications. In [14], a slot-coupled microstrip patch with four auxiliary patches was fed by a stripline. In [15] and [16], T-junction stripline feeding networks were employed to feed the subarrays. The stripline-based design offers the most degrees of freedom as it can be changed via the antenna design parameters, strip feed lines, and other design parameters. Because of the design flexibility, improved antenna performance, such as wide bandwidth, higher gain, and low sidelobe level, can be expected. However, the stripline fed-antenna design requires a comparatively complex and precise manufacturing process, which can be sensitive to fabrication errors. Thus, the effects of fabrication tolerances become more severe, and realization becomes more difficult as the frequency increases.

Multilayer SIW can be realized using the PCB fabrication process with vias and has been widely studied owing to its several advantages, including a low profile, low radiation loss, and low leakage from its sidewall [17], [18]. In [17], a slot-coupled aperture antenna was fed by SIW, and power dividers were implemented with SIW structures. In [18], the cavity and surrounding via fence were used to fabricate a feeding hollow waveguide and horn antenna on a multilayer LTCC substrate. Although the size of the antenna element was comparatively large, it was regarded as a sub-array antenna of the AiP owing to its advantages of high gain and wide bandwidth. The SIW approach is also preferred due to its simple structure because manufacturing errors affect the antenna performance. The interconnection structures from the RFIC to AiP can be realized using a dipole and via transition [19], [20], [21].

In this article, we discuss the advantages and challenges pertaining to designing scalable phased arrays of AiP in the 140-GHz frequency range. The next section reviews the existing scalable phased arrays and discusses the challenges of scalability in D-band applications. The prototype design considerations of a multilayered printed circuit board (PCB)-based AiPs are presented, which include a dual-polarized antenna element, a power divider (PD) design, and its sub-array structure. The design considerations and verification of a 4×4 array antenna with sub-array structures are discussed in the following section, and the conclusions are presented.

II. SCALABLE PHASED ARRAY ANTENNA MODULE

This section discusses the implementation of phased arrays and reviews scalable phased antenna arrays and scalability issues of D-band applications.

A. PHASED ARRAY MODULE IMPLEMENTATION

Scalable phased-antenna arrays can be implemented in several configurations; One is implementing antennas directly

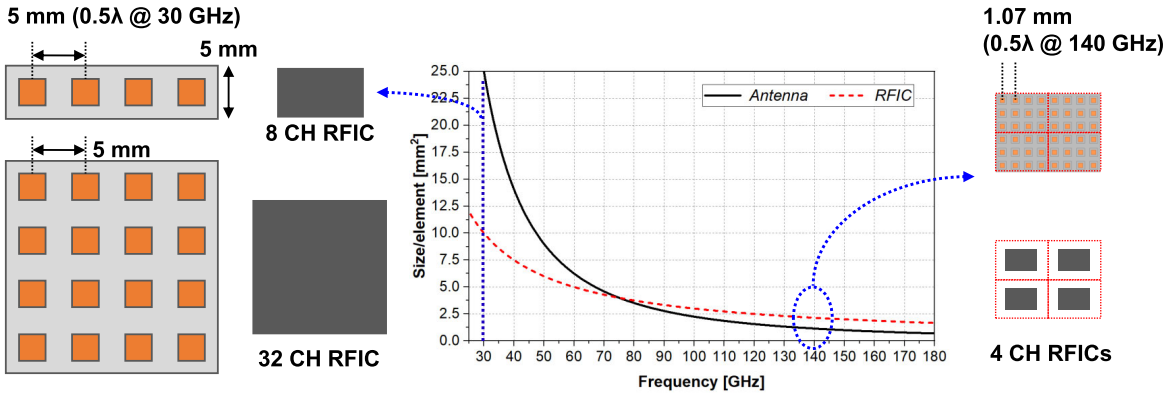

FIGURE 2. RFIC and antenna size according to frequency.

on a bare PCB. However, achieving sufficient antenna gain and bandwidth, particularly for D-band frequencies, is challenging due to coarse PCB manufacturing process and tolerances. Additionally, varying the number of unit modules according to the aperture size is not sufficiently flexible. Another implementing configuration of the scalable phased arrays based on AiP is illustrated in Fig. 1(a). A unit module consists of a PCB-embedded AiP and flip-chip bonded RFIC, as shown in Fig. 1(b). The modules can be mounted on the main PCB using ball-grid arrays (BGAs) to form a massive phased array. Numerous substrate technologies exist for implementing AiP depending on the application, including high-density interconnects, multilayered polymers, and low-temperature cofired ceramics (LTCC). The AiP configuration offers flexibility in terms of antenna design and testing, making it the most popular scaling approach [22], [23], [24], [25], [26], [27], [28], [29].

The other configuration that implements antennas directly on the RFIC wafer is referred to as an on-chip antenna [7], [30], [31]. Various types of on-chip antennas, including patches [32], slots [33], loops [34], [35], and dielectric resonator antennas [36], have been reported. Furthermore, an antenna with coupled feed radiators located on the superstrate can be designed; herein, the feed lines are designed with a metal layer of the RFIC [37], [38]. Additionally, using fan-out wafer-level packaging is another option [39]. Because the on-chip antenna reported higher efficiency, this approach is appealing as it can eliminate interconnection losses. However, there are still obstacles to address, including tackling thermal reliability concerns and establishing connections with the main PCB.

B. RFIC SIZE INCREASE AND ANTENNA APERTURE EFFICIENCY

Another issue is that the relative RFIC size increases compared with the N_T antenna elements as the frequency increases. As illustrated in Fig. 2, the area of the N_T AiP is proportional to the square of the antenna spacing. Thus, the antenna spacing of 5 mm and an area of 25 mm^2 at 30 GHz were reduced to 1 mm and 1 mm^2 at 150 GHz, respectively. However, the RFIC area did not diminish with λ^2 and was assumed to be proportional to $1/\lambda$ in Fig. 2 [6]. RFIC is typically smaller than AiP at lower mm-wave frequencies, for example, the $N_T \times N_T$ element transceiver (TRx) RFICs at 28 GHz can easily accommodate AiP [40], [41]. However, fitting the entire $N_T \times N_T$ RFICs in the area of the AiP becomes impossible as the frequency increases, as shown in Fig. 2. For example, phased arrays at 60 GHz and 94 GHz could not accommodate RFICs within the area of the AiP [14], [22]. The situation worsened for phased arrays at 150 GHz, and one TRx RFIC channel could be required to cover three or four antenna elements, because the area occupied by the BGAs became comparatively larger at higher frequencies.

Several attempts have been made to address the issue of the relative size reduction of the RFIC. In [22] and [23], dummy antennas were utilized to increase the size of the AiP to fit a dual-polarized TRx IC at 94 GHz. In the abovementioned study, the fill factor, or aperture efficiency, which is the ratio of the antenna area to the physical area, could be increased to 64%. However, this led to the occurrence of grating lobes, which distorted the shape of the sidelobes. In [14], two antenna pairs per front end, which is also referred to as the antenna sub-array, were employed in the elevation direction. As the aperture efficiency increased, the beam-scanning coverage became limited. The antenna spacing of the antenna pair was λ away from the adjacent antenna pair in the elevation direction, which caused the grating lobes. Despite the grating lobes and beam scanning limitations, antenna sub-array structures based on a PD design for AiP were proposed and designed in this study to maximize the aperture efficiency. Moreover, an improvement of $N_T^2 N_S$ in the EIRP for the N_T-array of the RFIC, $N_S N_R$ in the SNR for the N_R-array Rx could be anticipated with N_S sub-array.

III. PROTOTYPE OF AIP AT D-BAND

This section presents a prototype of the AiP design considerations and its challenges at the D-band for scalable

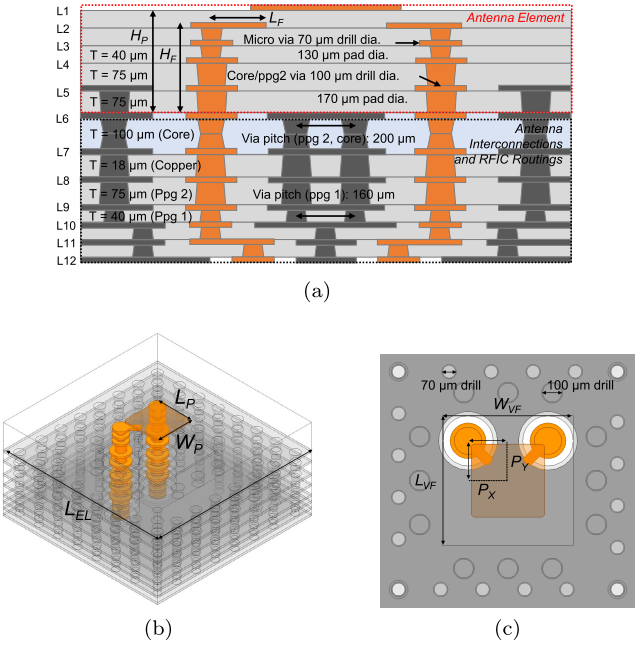

FIGURE 3. (a) Antenna layer structure in advanced multilayer PCB technology. (b) Bird's eye view of antenna element design. (c) Top view of antenna element design.

TABLE 1. The design parameters of the proposed antenna element.

Parameters	L_{EL}=W_{EL}	L_P=W_P	H_P	L_{VF}=W_{VF}	P_X=P_Y	H_F	L_F
Values (mm)	1.6	0.35	0.342	0.62	0.18	0.302	0.16

phased arrays, which includes a multilayered PCB-based dual-polarized antenna element, and two-stage PDs.

A. A DUAL-POLARIZED ANTENNA ELEMENT

A multilayered PCB manufacturing process has recently improved to handle D-band frequencies as illustrated in Fig. 3(a), which also shows the layer configuration of stripline-based sub-array structure of the AiP. Herein, a micro-via transition structure was utilized to implement an interconnection using flip-chip bonding between the RFIC and capture pad. The antenna feed also can be realized using a micro-via transition structure, and both direct and coupled feeding can be used. A bird's eye view and a top view of the proposed dual-polarized antenna element model are shown in Fig. 3(b) and (c). It consists of a patch with dimensions L_P and W_P, and coupled feeders with a height of H_F and length of L_F, as shown in Fig. 3, which are located at P_X and P_Y. A coupled feed patch antenna was designed for wide bandwidth and ±45° slant polarization. A via fence with dimensions L_{VF} and W_{VF}, and the ground plane with L_{EL} and W_{EL} are used. Table 1 lists all parameters of the proposed antenna in Fig. 3. The design parameters are adjusted to meet the design rules of multilayered PCB technology, such as minimum trace width and spacing, micro-via pitch, and diameter of the micro-via and pad in Fig. 3. As a multilayered PCB manufacturing process has matured, the latest technology can supply a

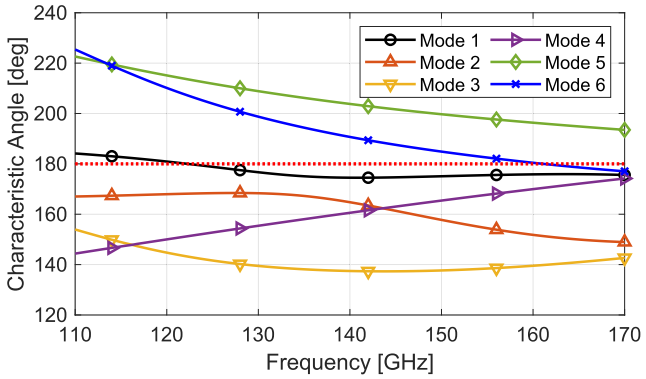

FIGURE 4. The modal significance of the proposed antenna.

minimum trace width and spacing of 30 μm. The micro-via and pad diameters vary depending on the thickness of the dielectric layers, as shown in Fig. 3(a) and (c). The steps of the fabrication process are introduced in [42]. The PCB consists of 12 layers and the relative dielectric permittivity (ε_r) of the core and prepreg substrate is 3.4 and 3.2, respectively, and the loss tangent of both substrates was 0.004 [43], [44].

B. ANTENNA OPERATING PRINCIPLE

Characteristic mode analysis (CMA) is a modal decomposition technique based on the method of moments (MoM). CMA enables the analysis of an antenna using only its structural properties [45], [46], [47], [48], [49]. The characteristic modes are identified by solving the following mathematical equations.

$$\vec{J} = \sum_n a_n J_n \tag{1}$$

where J_n is the characteristic current and a_n is the modal weighting coefficient.

$$a_n = \frac{V_n^i}{1 + j\lambda_n} \tag{2}$$

where λ_n represents the eigenvalue and V_n is the modal excitation coefficient. The modal significance, indicated as MS_n and measured by the normalized amplitude of the current modes, is calculated as follows:

$$MS_n = \left| \frac{1}{1 + j\lambda_n} \right| \tag{3}$$

The modal significance ranges from 0 to 1, with a mode reaching resonance when its modal significance, MS, is equal to 1. Furthermore, the characteristic angle (β_n) can be calculated as follows:

$$\beta_n = 180° - \tan^{-1}(\lambda_n) \tag{4}$$

It's noteworthy that when the characteristic angle falls within the range of 90° to 270°, a mode is in resonance when its characteristic angle equals 180°. Furthermore, the specific value of the characteristic angle indicates whether the mode is storing magnetic energy in an inductive mode

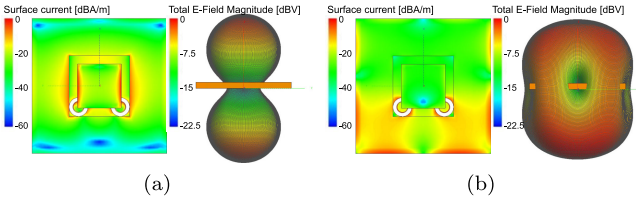

FIGURE 5. The current distribution and E-field patterns of each CMs. (a) J_1 at 120 GHz. (b) J_6 at 160 GHz.

(when $90° < a_n < 180°$) or storing electric energy in a capacitance mode (when $180° < a_n < 270°$).

CMA was used to analyze the antenna operation, and the characteristic modes of a simplified direct-fed patch antenna and the proposed antenna are achieved using Altair FEKO, as shown in Fig. 4. Six resonance modes were shown for each antenna structure with the characteristic angle. Two resonance modes can be found with the proposed antenna, and the CMs can be modified to expand the bandwidth, as shown in Fig. 4. It illustrates CMs that play a role in the radiation of the proposed antenna. Specific modes that contribute to the broadside radiation of the antenna have been chosen. The corresponding surface current distributions and E-field patterns are illustrated in Fig. 5. The surface currents are shown from a top view of the antenna, while the E-field patterns are plotted with a side view, showing their overlap with the ground. The CMs that resonate within the main patch are denoted as J_1, while those generated due to the interaction between the main patch and the feeder are labeled as J_6. As seen in Fig. 5(a) and (b), J_1 and J_6 exhibit current distributions with a $+45°$ slant polarization at 120 GHz and 160 GHz, respectively. This antenna design is tailored to efficiently excite these CMs, resulting in broadside radiation patterns across a wide frequency band.

Fig. 6(a) depicts the cross-section of the via transition from the lower metal layer to the upper layer. The capacitance of the cross-section shown in Fig. 6(a) are the pad barrel-to-plate coaxial capacitance, C_{BP}, and the via barrel-to-plate capacitance, C_{VP} [50], and these can be obtained by [43], [51], and [52]

$$C_{\mathrm{BP}} = \frac{2\pi\varepsilon_r\varepsilon_0 T}{\ln(D_{\mathrm{A}}/D_{\mathrm{PAD}})} \tag{5}$$

$$C_{\mathrm{VP}} = \frac{\pi\varepsilon_r\varepsilon_0 h B_0}{\ln(D_{\mathrm{A}}/D_{\mathrm{V}})} \tag{6}$$

where T and h are the thicknesses of the copper layer and substrate, and B_0 is the constant coefficient, respectively. Fig. 6(b) likely illustrates the equivalent circuit model of the multilayered via transitions and antenna element, where the via barrels are depicted as transmission lines with the impedance of the parallel plate (Z_{PP}). The design of the antenna element needs to consider the capacitance and impedance of this equivalent circuit model, and the anti-pad diameter (D_{A}), capture pad diameter (D_{PAD}), and via barrel diameter (D_{V}) play important roles in achieving the desired performance. Fig. 6(c) plots S-parameters of the equivalent

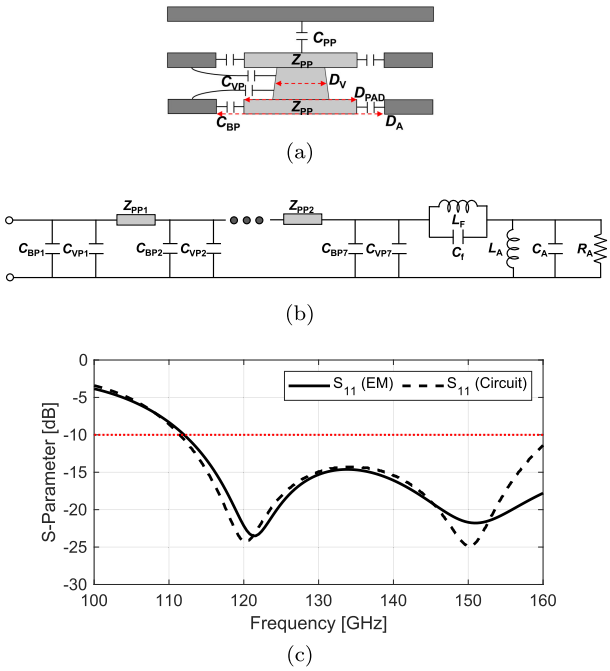

FIGURE 6. (a) A cross-section of the via transition from the lower metal layer to the upper layer. (b) An equivalent circuit model of the multilayered via transitions and antenna element. (c) Compared S-parameters of the circuit and EM simulation results.

circuit model and EM simulation results to validate the model.

The reactive impedance surface (RIS) structure is usually incorporated to achieve a wide bandwidth and a miniaturized patch size by expanding the tunable range of the input reactance [53], [54]. However, the RIS is used for the proposed antenna to increase the copper ratio, while maintaining antenna characteristics. The higher copper ratio can prevent warpage of the fabricated AiP module. Small patches with dimensions of W_{RIS} and G_{RIS} are periodically allocated from layer 2 to 4, as illustrated in Fig. 7(a) and (b). In addition, some of the RIS are removed with $W_{\mathrm{R}} = L_{\mathrm{R}} = 0.94$ mm to prohibit unintended distortion of the radiation pattern. In Fig. 7(a), S-parameters are presented with a fixed $G_{\mathrm{RIS}} = 0.03$ mm a variation in the size of W_{RIS}. The bandwidth of the S_{11} is maintained with RIS, and S_{21} can be enhanced for the lower frequency.

The radiation patterns for $\phi = 0°$ and $90°$ of the proposed antenna element are illustrated in Fig. 8(b) and (c). Although the array antenna spacing is 1.2 mm, the width and length of the element ground plane are determined as 1.6 mm, $0.75\lambda_0$ at 140 GHz to provide suitable antenna element gain. The radiation pattern and antenna gain can be retained for various size of multilayered RIS. The simulation results at 140 GHz shows the realized gain of approximately 5.5 dBi, radiation efficiency of approximately 94%, and the half-power beam widths (HPBW) of approximately 83°. As shown in Fig. 8(b) and 8(c), despite the tilting of the radiation patterns due to the asymmetry of the coupled patch's

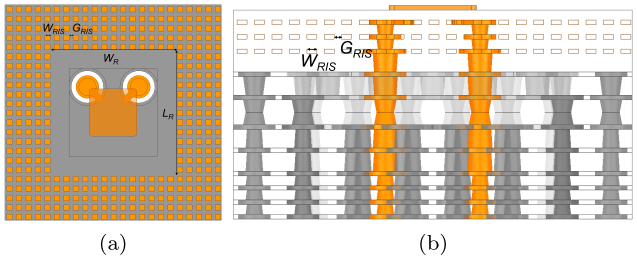

FIGURE 7. (a) Top view of antenna element with RIS. (b) Cross-sectional view of antenna element with RIS.

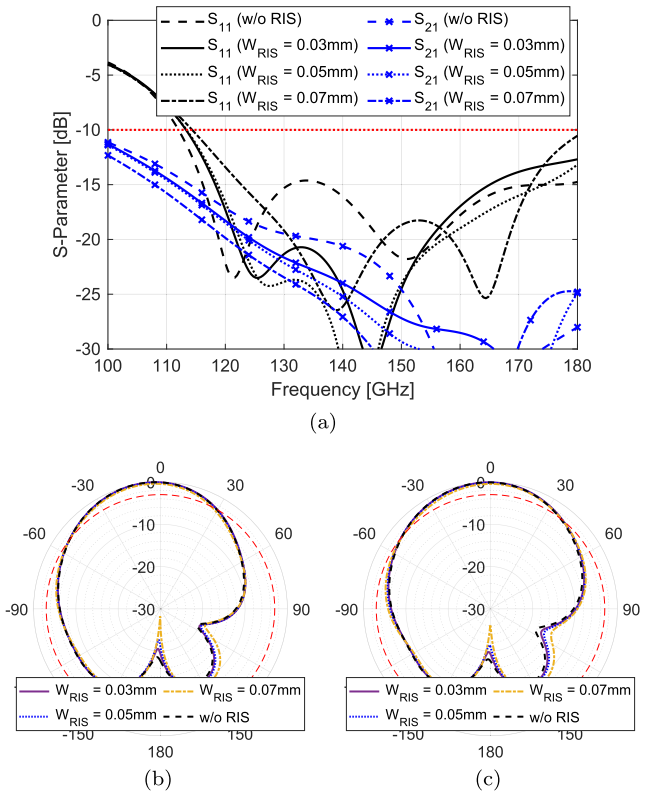

FIGURE 8. (a) The simulated S-parameters of the proposed antenna according to the size of RIS. The simulated radiation patterns of proposed antenna element at 140 GHz. (b) $\phi = 0°$ and (c) $\phi = 90°$.

feeding structure, the −6 dB beam is still capable of covering an angle of ±60°.

IV. POWER DIVIDER AND SUB-ARRAY DESIGN

This section presents two stage PDs, which can be used for sub-array antenna implementation. Two types of PDs are designed and configured 4 × 1 sub-array with antenna elements.

A. POWER DIVIDER DESIGN

The two stage PDs are designed with striplines on layer 11 to configure four sub-array antennas, as illustrated in Fig. 9(a) and (b). Type A PD in Fig. 9(a) employs two stage T-junction PDs to split the input signal into four antenna ports, which has a conventional T-junction PD composed with

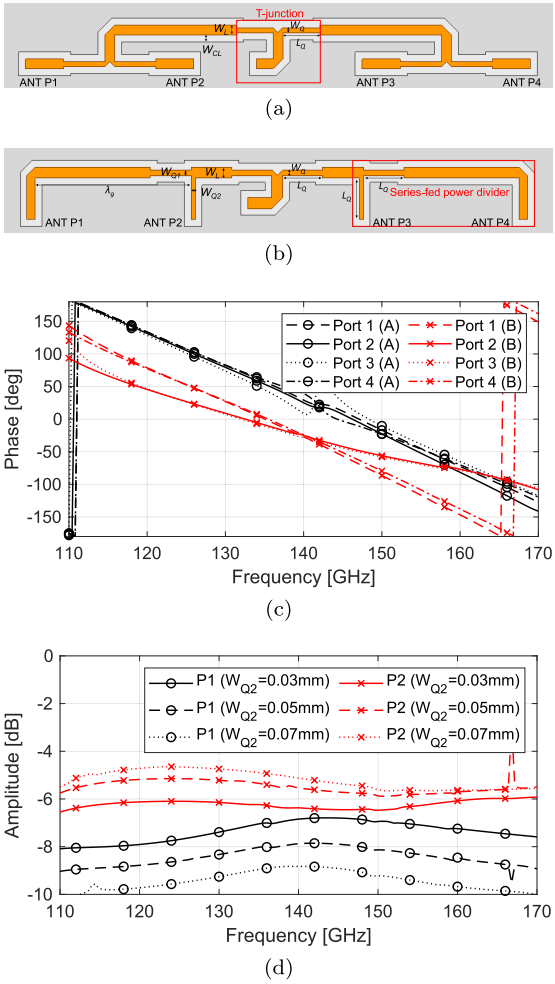

FIGURE 9. (a) Top view of PD Type A. (b) Top view of PD Type B. (c) The simulated phase of each antenna ports for two PDs. (c) The simulated amplitude of each antenna ports for PD Type B.

quarter-wave transformers [55]. Although the Type A PD can provide the in-phased output signals with same length of routings, as shown in Fig. 9(c), the insertion loss can be increased because of detoured lines. Whereas Type B PD in Fig. 9(b) utilize a T-junction PD and series-fed PD [13], [56], [57]. The Type B PD is proposed to have the advantages of compact configuration, lower insertion loss, and simple variation of the number of antenna ports which can be extended by attaching a series-fed PD. Herein, a series-fed PD consists of two quarter-wave transformers and the 50Ω impedance lines. To make phase of the output signals equal, the difference of line length between the antenna ports are determined to λ_g which is approximately 1.2 mm at 140 GHz center frequency. However, the phase difference between the antenna ports is increased with frequency variation, as shown in Fig. 9(c). The amplitude of the antenna port 1 and port 2 are inversely proportional to the impedance of the quarter-wave transformers which is given by

$$\frac{a_1}{a_2} = \frac{Z_2}{Z_1} = \frac{W_{Q1}}{W_{Q2}} \tag{7}$$

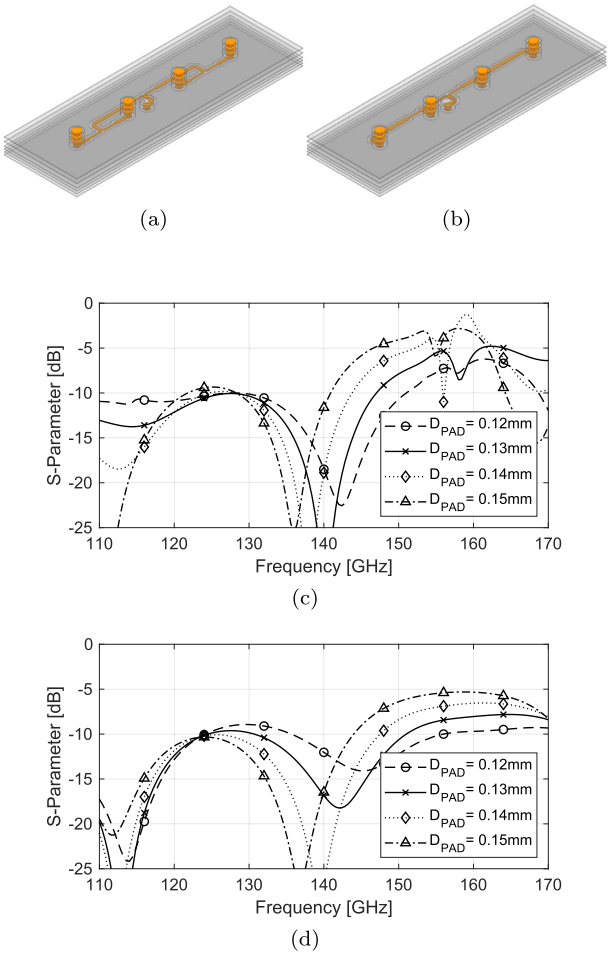

FIGURE 10. Bird's eye view of the PD with transition. (a) Type A (b) Type B. The simulated S_{11} of PDs. (c) Type A. (d) Type B.

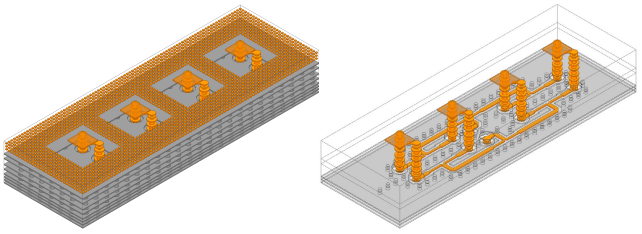

FIGURE 11. Bird's eye view of four sub-array antenna with and without multi-RIS and ground planes.

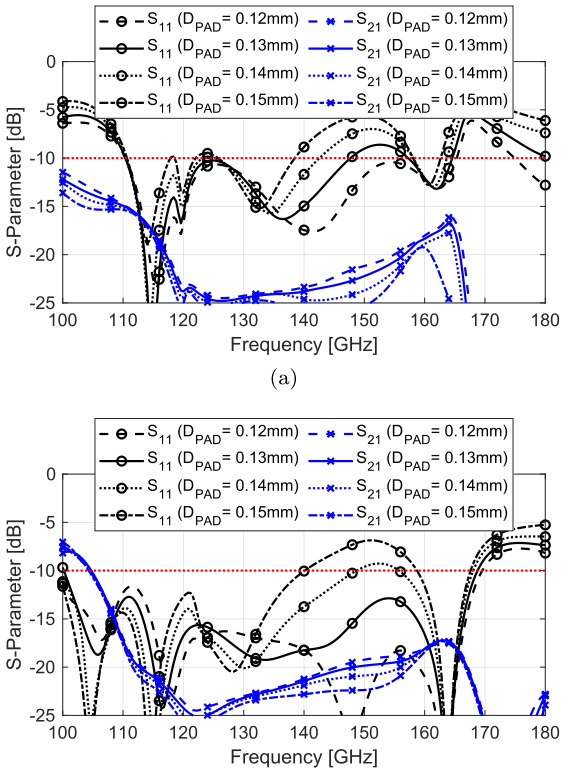

FIGURE 12. The simulated S-parameters of antenna sub-array according to the variation of a capture pad diameter. (a) Type A. (b) Type B.

where W_{Q1} and W_{Q2} are width of quarter-wave transformers which are shown in Fig. 9(b). The amplitudes of each ports can be adjusted with widths of the lines, and the amplitudes of port 1 and 2 are plotted for a fixed $W_{Q1} = 0.4$ mm and varied W_{Q2}, in Fig. 9(d). Although the amplitude of port 1 can be increased with decrease of W_{Q2}, the amplitude is smaller than -6 dB because of the insertion loss. In addition, the antenna sub-array can be designed to have low side-lobe level by applying proper amplitude such as Chebychev tapered distribution. For the sub-array antenna constitution, a transition structure with circular pads and micro-vias are connected to the PDs, as illustrated in Fig. 10(a) and (b). From the S_{11} of the PD with transition as shown in Fig. 10(c) and (d), the S_{11} is deteriorated with increase of D_{PAD} and the capacitance, which can be obtained by (1).

B. SUB-ARRAY ANTENNA DESIGN

A four sub-array antenna was designed with the combination of the proposed antenna element and PDs, as shown in Fig. 11. A bird's eye view is illustrated with and without multi-RIS and ground planes. By transitioning using circular pads and micro-vias, it is possible to interconnect from four patch antennas on layer 1 to input port on layer 12 which can be attached to an RFIC. Both Type A and Type B PDs are designed and optimized to achieve wide impedance bandwidth, wide gain bandwidth, and higher port-to-port isolation. Fig. 12(a) and (b) shows the S-parameters of antenna sub-array according to the variation of a capture pad diameter, respectively. Although Type A PD could achieve 39% bandwidth with $D_{PAD} = 0.12$ mm, it was revised to $D_{PAD} = 0.13$ mm because of PCB manufacturing margin, and the bandwidth reduced to approximately 28%. While the S_{11} was sensitive to the size of a capture pad and micro-via, S_{21} could be stably attained which was smaller than -15dB for the entire bandwidth. In the case of Type B PD with $D_{PAD} = 0.13$ mm, S_{11} of approximately 42.8% bandwidth and S_{21} smaller than -15 dB could be achieved.

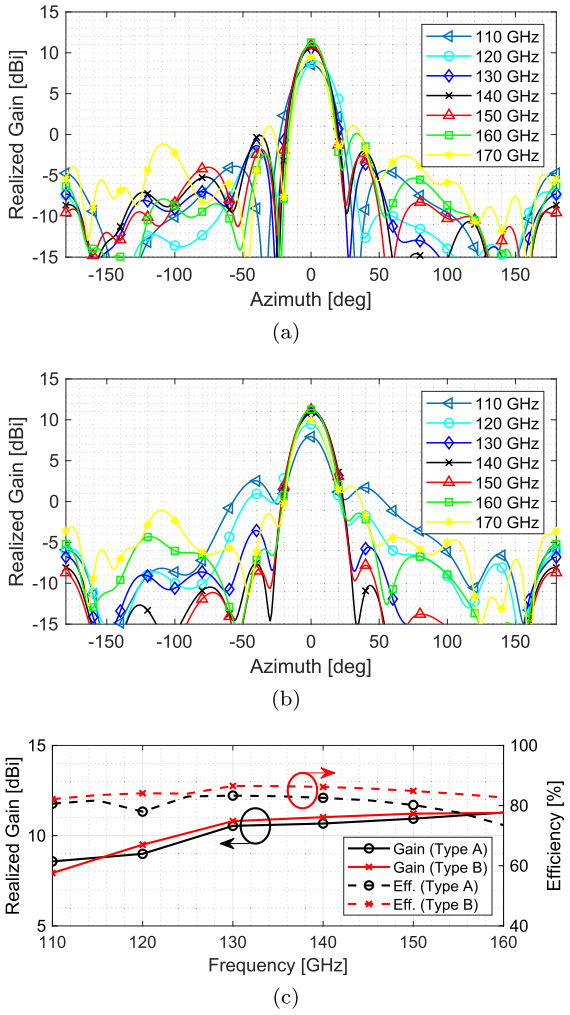

FIGURE 13. The simulated radiation patterns with frequency variation of (a) Sub-array Type A. (b) Sub-array Type B. (c) A maximum realized gain and efficiency of the sub-array antennas according to frequency.

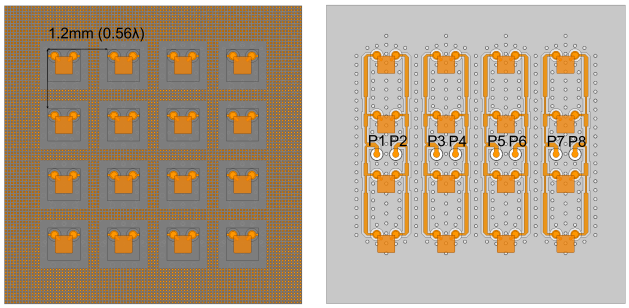

FIGURE 14. Top view of 4 × 4 antenna array design.

The element spacing was also determined to be 1.2 mm, and PD was symmetrically arranged to prevent the squint of broadside beam direction which can be occurred because of phase difference of each antenna ports from varying with frequency. In addition, the cross-polarization discrimination (XPD) of the array can be improved. The radiation patterns of the antenna array are plotted from 110 to 170 GHz

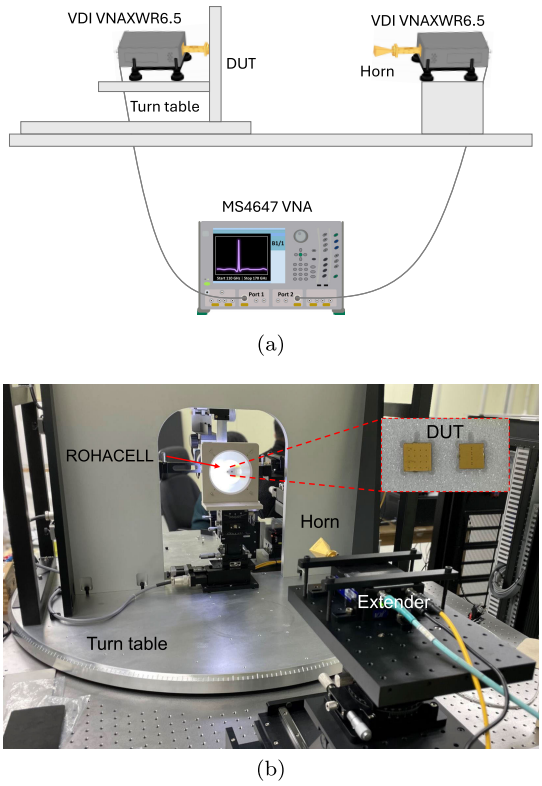

FIGURE 15. Vertically mountable measurement setup. (a) An illustrative block diagram. (b) A photograph of the backside and fabricated odules.

for every 10 GHz, as shown in Fig. 13(a) and (b). From the radiation patterns in the figures, the maximum gain is approximately 11 dBi and the HPBW is approximately 25° at 140 GHz for the two cases. Although the squint of the beam direction can be avoided with symmetrical design, the distortion of the radiation pattern occurs at the lowest and highest operating frequencies. However, the 3 dB gain bandwidth is over 43% which can cover D-band frequency, as shown in Fig. 13(c).

V. ARRAY ANTENNA DESIGN AND VALIDATION

A 4 × 4 antenna array with four sub-array was designed to verify the antenna sub-array and array performance of two PDs. The simulation model for the antenna array design using Type B PD is shown in Fig. 14. In this design, the spacing between sub-array antennas is set to be 1.2 mm. Eight antenna ports are included in the design, with circular pads for measurements using ground-signal-ground (GSG) probes.

A. S-PARAMETER MEASUREMENTS

Fig. 15 presents the setup configuration and a photo of the measurement setup and fabricated AiP modules used for validation. To the best of the authors' knowledge, this is the first vertically mountable measurement setup for D-band frequencies that incorporates waveguide and frequency extension units. The setup comprises a vector network analyzer (VNA), waveguide-connected GSG probes,

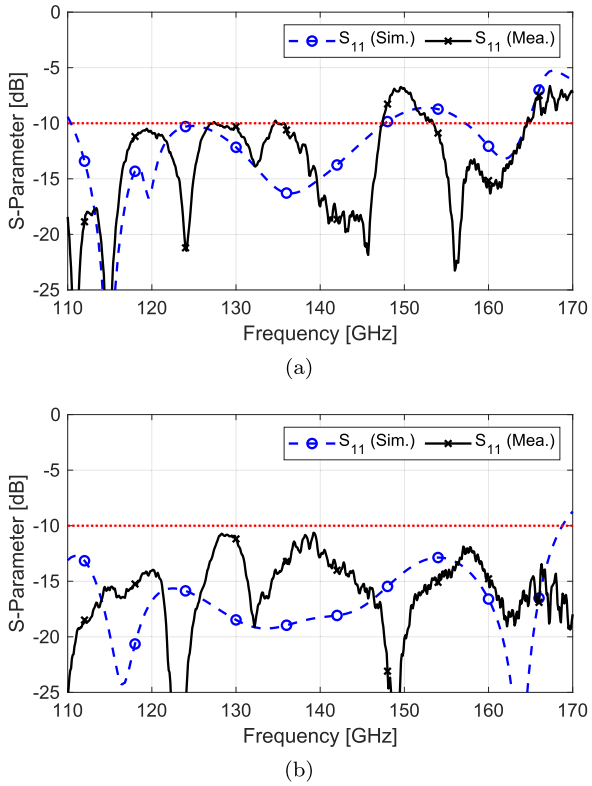

FIGURE 16. Compared S-parameters. (a) Array antenna Type A. (b) Array antenna Type B.

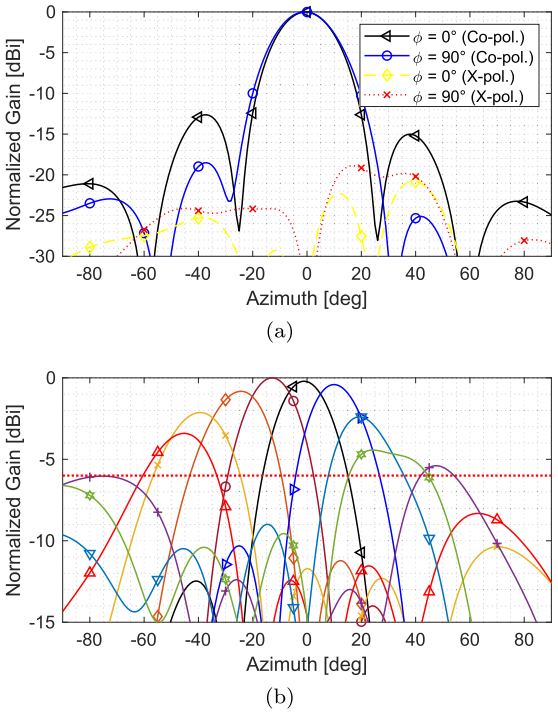

FIGURE 17. Radiation patterns of the array antenna Type B at 140 GHz. (a) Co-pol. and X-pol. beams (b) Beamforming performance.

and frequency extension units. With the frequency extension unit enabling VNA operation from 110 to 170 GHz, the measurement capability extends to D-band frequencies. Traditional D-band measurements often involve planar probe stations due to the presence of bulky frequency extension units and waveguides. However, such configurations come with constraints, such as limited assessment scope for radiation pattern evaluations and the capacity to measure solely within the same plane using the GSG probe. To overcome these limitations, a vertically mountable arrangement incorporating the extender, waveguide, and GSG probes has been implemented, as depicted in Fig. 15(a) and (b). Additionally, two types of PDs for 4 × 4 antenna array modules were fabricated to verify the antenna designs in the previous sections. Calibration and measurement of the modules were carried out on a ROHACELL foam. The measured S-parameters closely resembled the simulation results, as depicted in Fig. 16(a) and (b). S_{11} of the measured results achieved a bandwidth of approximately 40 GHz (28.5%) and 60 GHz (42.8%), respectively.

B. RADIATION PATTERN VALIDATION

The simulated co-polarization and cross-polarization radiation patterns of the 4 × 4 antenna array using Type B PD are depicted at 140 GHz for $\phi = 0°$ and 90° in Fig. 17(a). At this frequency, the 4 × 4 antenna array achieves a maximum gain of 16.7 dBi, a radiation efficiency of approximately 80.7%, and a cross-polarization discrimination (XPD) exceeding 20 dB. Additionally, the antenna array exhibits peak gains of 16.4 dBi at 120 GHz and 17.2 dBi at 140 GHz. Fig. 17(b) illustrates the beamforming performances of the antenna array, revealing a 6 dB antenna coverage (red dashed line) wider than 110°.

To verify the radiation pattern, a vertically mountable measurement setup was established. The setup involves a VNA, GSG probes, and frequency extension units, with a fixed horn antenna, as depicted in Fig. 15. The measurement angle can be automatically adjusted from −65° to 65° using a turntable. Fig. 18(a), (b), and (c) display the measured radiation patterns of sub-array antenna elements at 120, 140, and 160 GHz, respectively, demonstrating close resemblance to the simulated results. The radiation patterns are normalized based on the simulated result at the boresight ($\phi = \theta = 0°$). The elevation radiation results ($\phi = 0°$) indicate that the half-power beamwidth (HPBW) of the sub-array design reaches a maximum of approximately 70°. However, the wide spacing between sub-array elements may limit the beamforming scanability.

While sub-array designs are commonly utilized in massive multiple-input multiple-output base stations, D-band applications may necessitate broader coverage due to their short-range characteristics. In such scenarios, additional technologies like reconfigurable transmitarrays or metasurfaces can be employed. A reconfigurable metasurface typically comprises multiple unit cells capable of manipulating the phase of electromagnetic waves to enhance antenna coverage

TABLE 2. Comparison of sub-array structures of AiP.

Ref. No.	No. of Array	Dimension ($\lambda_0 \times \lambda_0$)	f_0 (GHz)	BW (%)	Peak Gain (dBi)	3 dB Gain BW (%)	Efficiency (%)	Technology
[15]	4×4	5.6×5.6	140	7.1	18.8	7.9	65	LTCC
[16]	2×2	1.63×1.63	122	3.3	12.2	92	80	LTCC
[25]	6×8	2.82×4.48	60	15	29.5	-	-	LTCC
[28]	4×4	2×2	145	13.8	14	14	71	Layered PCB
[29]	4×4	3×3	140	25	17.5	25	80	Layered PCB
This work	4×4	2.4×2.4	140	42.8	16.7	43	81	Layered PCB

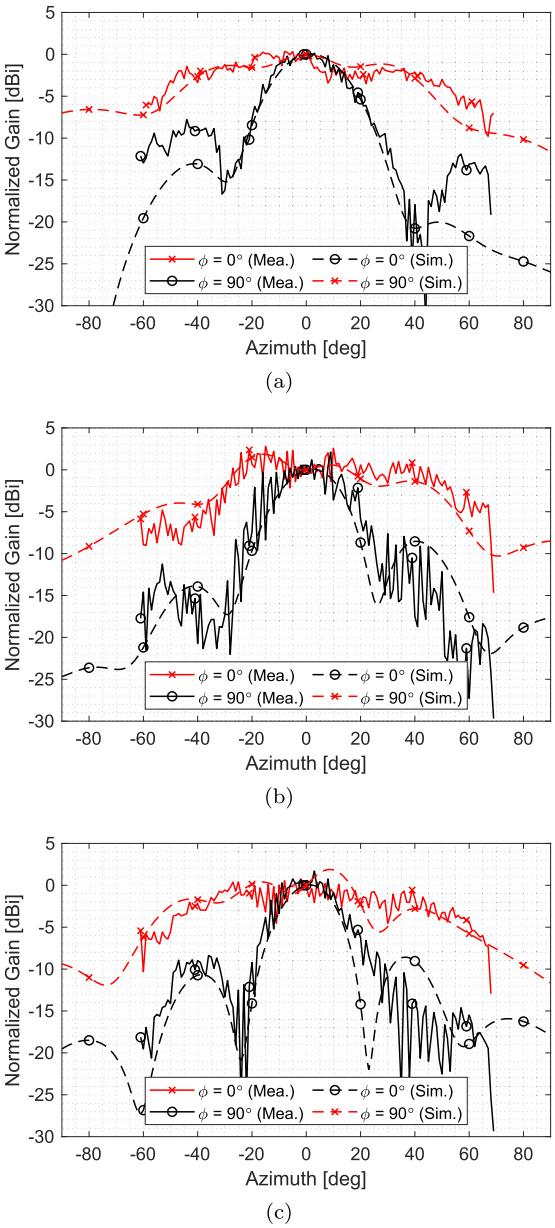

FIGURE 18. Compared radiation patterns of the sub-array antenna element. (a) 120 GHz. (a) 140 GHz. (a) 160 GHz.

or gain. Unit cells can be implemented using various methods, including PIN diodes, varactors, and liquid crystals (LC). Other technologies, such as reconfigurable beam-steering and LC-based leaky wave holographic antennas, can also be applied to achieve additional beamforming coverage.

C. COMPARISON WITH PREVIOUS STUDIES

Table 2 compares the proposed antenna's performance with previously studied sub-array structures of AiP. The figure of merit was evaluated based on the number of antenna arrays, dimension, center frequency, −10 dB impedance bandwidth, maximum antenna gain, 3 dB gain bandwidth, efficiency, and fabrication technology. The proposed antenna array has an impedance bandwidth of more than 42.8%, which is relatively wide compared with those reported in previous studies. In addition, the maximum gain in this work is higher than that of the other antennas.

VI. CONCLUSION

Phased array antennas are increasingly being utilized across diverse domains such as satellite and wireless communications, radars, and imaging. This paper delves into the benefits and hurdles encountered in designing scalable phased arrays operating at D-band frequencies. We discuss the key considerations for implementing Antenna-in-Package (AiP) using stripline technology. Subsequently, we propose a sub-array structure based on stripline phase shifters for AiP at D-band, achieving significant milestones including a 42.8% impedance bandwidth, port-to-port isolation exceeding 15 dB, and a 3 dB gain bandwidth of 43%. Furthermore, we design a 4×4 antenna array to evaluate the scalability of AiP for phased arrays, showcasing impressive characteristics such as a maximum gain of 16.7 dBi, a radiation efficiency of 80.7%, and an XPD surpassing 20 dB. Experimental findings validate the −10 dB impedance bandwidth of about 42.8% and radiation patterns. In summary, our proposed sub-array structure for stripline phase shifter-based AiP at D-band exhibits promising performance for scalable phased arrays, with experimental results corroborating the design's efficacy. This research contributes to advancing D-band phased array antennas and their potential applications across diverse communication and sensing systems.

REFERENCES

[1] S. Dang, O. Amin, B. Shihada, and M.-S. Alouini, "What should 6G be?" *Nature Electron.*, vol. 3, no. 1, pp. 20–29, Jan. 2020.

[2] Samsung Research. (May 5, 2022). *6G Spectrum Expanding the Frontier*. [Online]. Available: https://cdn.codeground.org/nsr/downloads/researchareas/2022May_6G_Spectrum.pdf
[3] J. Edwin, "FCC opens spectrum horizons for new services and technologies," Docket, Tech. Rep., 2019, pp. 18–21.
[4] R. Eva, A. Gustavo, M. Jose, and G. Pedro, "Atmospheric attenuation in wireless communication systems at millimeter and THz frequencies," *IEEE Antennas Propag. Mag.*, vol. 57, no. 1, pp. 48–61, Feb. 2015.
[5] J. J. Lee, "G/T and noise figure of active array antennas," *IEEE Trans. Antennas Propag.*, vol. 41, no. 2, pp. 241–244, Feb. 1993.
[6] B. Sadhu, X. Gu, and A. Valdes-Garcia, "The more (antennas), the merrier: A survey of silicon-based mm-wave phased arrays using multi-IC scaling," *IEEE Microw. Mag.*, vol. 20, no. 12, pp. 32–50, Dec. 2019.
[7] K.-Q. Huang and M. Swaminathan, "Antennas in glass interposer for sub-THz applications," in *Proc. IEEE 71st Electron. Compon. Technol. Conf. (ECTC)*, Jun. 2021, pp. 1150–1155.
[8] H. Sherry, R. A. Hadi, J. Grzyb, E. Öjefors, A. Cathelin, A. Kaiser, and U. R. Pfeiffer, "Lens-integrated THz imaging arrays in 65nm CMOS technologies," in *Proc. IEEE Radio Freq. Integr. Circuits Symp.*, Jun. 2011, pp. 1–4.
[9] W. Menzel and A. Moebius, "Antenna concepts for millimeter-wave automotive radar sensors," *Proc. IEEE*, vol. 100, no. 7, pp. 2372–2379, Jul. 2012.
[10] R. Hasan, W. A. Ahmed, J.-H. Lu, H. J. Ng, and D. Kissinger, "*F*-band differential microstrip patch antenna array and waveguide to differential microstrip line transition for FMCW radar sensor," *IEEE Sensors J.*, vol. 19, no. 15, pp. 6486–6496, Aug. 2019.
[11] J. Xu, W. Hong, H. Zhang, G. Wang, Y. Yu, and Z. H. Jiang, "An array antenna for both long- and medium-range 77 GHz automotive radar applications," *IEEE Trans. Antennas Propag.*, vol. 65, no. 12, pp. 7207–7216, Dec. 2017.
[12] S. Beer, H. Gulan, C. Rusch, and T. Zwick, "Coplanar 122-GHz antenna array with air cavity reflector for integration in plastic packages," *IEEE Antennas Wireless Propag. Lett.*, vol. 11, pp. 160–163, 2012.
[13] D. M. Pozar and D. H. Schaubert, "Comparison of three series fed microstrip array geometries," in *Proc. IEEE Antennas Propag. Soc. Int. Symp.*, vol. 2, Jul. 1993, pp. 728–731.
[14] T. Sowlati et al., "A 60GHz 144-element phased-array transceiver with 51dBm maximum EIRP and ±60° beam steering for backhaul application," in *IEEE Int. Solid-State Circuits Conf. (ISSCC) Dig. Tech. Papers*, Feb. 2018, pp. 66–68.
[15] B. Zhang, H. Gulan, T. Zwick, Y. Li, U. Oderfält, F. Carlsson, and H. Zirath, "Integration of a 140 GHz packaged LTCC grid array antenna with an InP detector," *IEEE Trans. Compon., Packag. Manuf. Technol.*, vol. 5, no. 8, pp. 1060–1068, Aug. 2015.
[16] A. Bhutani, B. Göttel, A. Lipp, and T. Zwick, "Packaging solution based on low-temperature cofired ceramic technology for frequencies beyond 100 GHz," *IEEE Trans. Compon., Packag. Manuf. Technol.*, vol. 9, no. 5, pp. 945–954, May 2019.
[17] J. Xu, Z. N. Chen, X. Qing, and W. Hong, "140-GHz planar broadband LTCC SIW slot antenna array," *IEEE Trans. Antennas Propag.*, vol. 60, no. 6, pp. 3025–3028, Jun. 2012.
[18] T. Tajima, H.-J. Song, K. Ajito, M. Yaita, and N. Kukutsu, "300-GHz step-profiled corrugated horn antennas integrated in LTCC," *IEEE Trans. Antennas Propag.*, vol. 62, no. 11, pp. 5437–5444, Nov. 2014.
[19] T. Tajima, H.-J. Song, H. Matsuzaki, and M. Yaita, "LTCC-integrated *H*-plane bends for THz antenna-in-package solution," *IEEE Microw. Wireless Compon. Lett.*, vol. 27, no. 5, pp. 440–442, May 2017.
[20] S. Hu, Y.-Z. Xiong, B. Zhang, L. Wang, T.-G. Lim, M. Je, and M. Madihian, "A SiGe BiCMOS transmitter/receiver chipset with on-chip SIW antennas for terahertz applications," *IEEE J. Solid-State Circuits*, vol. 47, no. 11, pp. 2654–2664, Nov. 2012.
[21] J. Choi, J. Park, Y. Youn, W. Hwang, H. Seong, Y. N. Whang, and W. Hong, "Frequency-adjustable planar folded slot antenna using fully integrated multithrow function for 5G mobile devices at millimeter-wave spectrum," *IEEE Trans. Microw. Theory Techn.*, vol. 68, no. 5, pp. 1872–1881, May 2020.
[22] X. Gu, A. Valdes-Garcia, A. Natarajan, B. Sadhu, D. Liu, and S. K. Reynolds, "W-band scalable phased arrays for imaging and communications," *IEEE Commun. Mag.*, vol. 53, no. 4, pp. 196–204, Apr. 2015.
[23] X. Gu, D. Liu, C. Baks, J.-O. Plouchart, W. Lee, and A. Valdes-Garcia, "An enhanced 64-element dual-polarization antenna array package for W-band communication and imaging applications," in *Proc. IEEE 68th Electron. Compon. Technol. Conf. (ECTC)*, May 2018, pp. 197–201.
[24] S. Shahramian, M. J. Holyoak, and Y. Baeyens, "A 16-element W-band phased-array transceiver chipset with flip-chip PCB integrated antennas for multi-gigabit wireless data links," *IEEE Trans. Microw. Theory Techn.*, vol. 66, no. 7, pp. 3389–3402, Jul. 2018.
[25] T. Sowlati et al., "A 60-GHz 144-element phased-array transceiver for backhaul application," *IEEE J. Solid-State Circuits*, vol. 53, no. 12, pp. 3640–3659, Dec. 2018.
[26] S. Pellerano, S. Callender, W. Shin, Y. Wang, S. Kundu, A. Agrawal, P. Sagazio, B. Carlton, F. Sheikh, A. Amadjikpe, W. Lambert, D. S. Vemparala, M. Chakravorti, S. Suzuki, R. Flory, and C. Hull, "A scalable 71-to-76GHz 64-element phased-array transceiver module with 2×2 direct-conversion IC in 22nm FinFET CMOS technology," in *Proc. IEEE Int. Solid- State Circuits Conf. - (ISSCC)*, Feb. 2019, pp. 174–176.
[27] W. J. Lambert, A. L. Amadjikpe, J. Yao, S. C. J. Chavali, P. Sagazio, Y. S. Nam, M. Abu-Mahaimed, and S. Pellerano, "Scalable multichip packaging with integrated antenna array for a 73-GHz transceiver IC," *IEEE Trans. Microw. Theory Techn.*, vol. 69, no. 1, pp. 387–398, Jan. 2021.
[28] A. Lamminen, J. Säily, J. Ala-Laurinaho, J. de Cos, and V. Ermolov, "Patch antenna and antenna array on multilayer high-frequency PCB for D-band," *IEEE Open J. Antennas Propag.*, vol. 1, pp. 396–403, 2020.
[29] T. Dao, A. Kearns, D. R. Paredes, and G. Hueber, "Wideband high-gain stacked patch antenna array on standard PCB for D-band 6G communications," *IEEE Antennas Wireless Propag. Lett.*, vol. 23, pp. 478–482, 2024.
[30] H. M. Cheema and A. Shamim, "The last barrier: On-chip antennas," *IEEE Microw. Mag.*, vol. 14, no. 1, pp. 79–91, Jan. 2013.
[31] M. de Kok, A. B. Smolders, and U. Johannsen, "A review of design and integration technologies for D-band antennas," *IEEE Open J. Antennas Propag.*, vol. 2, pp. 746–758, 2021.
[32] Y. Tousi and E. Afshari, "A scalable THz 2D phased array with +17dBm of EIRP at 338GHz in 65nm bulk CMOS," in *IEEE Int. Solid-State Circuits Conf. (ISSCC) Dig. Tech. Papers*, Feb. 2014, pp. 258–259.
[33] D. Hou, Y.-Z. Xiong, W.-L. Goh, S. Hu, W. Hong, and M. Madihian, "130-GHz on-chip meander slot antennas with stacked dielectric resonators in standard CMOS technology," *IEEE Trans. Antennas Propag.*, vol. 60, no. 9, pp. 4102–4109, Sep. 2012.
[34] K. Sengupta and A. Hajimiri, "A 0.28 THz power-generation and beam-steering array in CMOS based on distributed active radiators," *IEEE J. Solid-State Circuits*, vol. 47, no. 12, pp. 3013–3031, Dec. 2012.
[35] S. Sengupta, D. R. Jackson, and S. A. Long, "A method for analyzing a linear series-fed rectangular microstrip antenna array," *IEEE Trans. Antennas Propag.*, vol. 63, no. 8, pp. 3731–3736, Aug. 2015.
[36] N. Buadana, S. Jameson, and E. Socher, "A multiport chip-scale dielectric resonator antenna for CMOS THz transmitters," *IEEE Trans. Microw. Theory Techn.*, vol. 68, no. 9, pp. 3621–3632, Sep. 2020.
[37] W. Shin, O. Inac, Y.-C. Ou, B. Ku, and G. M. Rebeiz, "A 108–112 GHz 4×4 wafer-scale phased array transmitter with high-efficiency on-chip antennas," in *Proc. IEEE Radio Freq. Integr. Circuits Symp.*, Jun. 2012, pp. 199–202.
[38] S. Zihir, O. D. Gurbuz, A. Kar-Roy, S. Raman, and G. M. Rebeiz, "60-GHz 64- and 256-elements wafer-scale phased-array transmitters using full-reticle and subreticle stitching techniques," *IEEE Trans. Microw. Theory Techn.*, vol. 64, no. 12, pp. 4701–4719, Dec. 2016.
[39] B. Yu, Z. Qian, C. Lin, J. Lin, Y. Zhang, G. Yang, and Y. Luo, "A wideband mmWave antenna in fan-out wafer level packaging with tall vertical interconnects for 5G wireless communication," *IEEE Trans. Antennas Propag.*, vol. 69, no. 10, pp. 6906–6911, Oct. 2021.
[40] J. D. Dunworth, A. Homayoun, B-H. Ku, Y-C. Ou, K. Chakraborty, G. Liu, T. Segoria, J. Lerdworatawee, J. W. Park, H-C. Park, H. Hedayati, D. Lu, P. Monat, K. Douglas, and V. Aparin, "A 28GHz bulk-CMOS dual-polarization phased-array transceiver with 24 channels for 5G user and basestation equipment," in *IEEE Int. Solid-State Circuits Conf. (ISSCC) Dig. Tech. Papers*, Feb. 2018, pp. 70–72.
[41] B. Sadhu et al., "A 28-GHz 32-element TRX phased-array IC with concurrent dual-polarized operation and orthogonal phase and gain control for 5G communications," *IEEE J. Solid-State Circuits*, vol. 52, no. 12, pp. 3373–3391, Dec. 2017.

[42] H. Aliakbari, M. Mosalanejad, C. Soens, G. A. E. Vandenbosch, and B. K. Lau, "Wideband SIW-based low-cost multilayer slot antenna array for *E*-band applications," *IEEE Trans. Compon., Packag. Manuf. Technol.*, vol. 9, no. 8, pp. 1568–1575, Aug. 2019.
[43] H. Kim and J. Oh, "140-GHz wideband array antenna-in-package using multimode resonance," *IEEE Trans. Antennas Propag.*, vol. 71, no. 3, pp. 2136–2144, Mar. 2023.
[44] H. Kim, J. Jung, W. Lee, S. Nam, and J. Oh, "D-band 4×4 multi-feed array antenna-in-package for high-power combining and polarization synthesis," *IEEE Access*, vol. 11, pp. 144006–144016, 2023.
[45] M. Cabedo-Fabres, E. Antonino-Daviu, A. Valero-Nogueira, and M. Bataller, "The theory of characteristic modes revisited: A contribution to the design of antennas for modern applications," *IEEE Antennas Propag. Mag.*, vol. 49, no. 5, pp. 52–68, Oct. 2007.
[46] M. Vogel, G. Gampala, D. Ludick, U. Jakobus, and C. J. Reddy, "Characteristic mode analysis: Putting physics back into simulation," *IEEE Antennas Propag. Mag.*, vol. 57, no. 2, pp. 307–317, Apr. 2015.
[47] J. J. Borchardt and T. C. Lapointe, "U-slot patch antenna principle and design methodology using characteristic mode analysis and coupled mode theory," *IEEE Access*, vol. 7, pp. 109375–109385, 2019.
[48] B. B. Q. Elias, P. J. Soh, A. A. Al-Hadi, P. Akkaraekthalin, and G. A. E. Vandenbosch, "A review of antenna analysis using characteristic modes," *IEEE Access*, vol. 9, pp. 98833–98862, 2021.
[49] G. Kim and S. Kim, "Design and analysis of dual polarized broadband microstrip patch antenna for 5G mmWave antenna module on FR4 substrate," *IEEE Access*, vol. 9, pp. 64306–64316, 2021.
[50] G. Hernandez-Sosa, R. Torres-Torres, and A. Sanchez, "Impedance matching of traces and multilayer via transitions for on-package links," *IEEE Microw. Wireless Compon. Lett.*, vol. 21, no. 11, pp. 595–597, Nov. 2011.
[51] I. Ndip, F. Ohnimus, K. Löbbicke, M. Bierwirth, C. Tschoban, S. Guttowski, H. Reichl, K.-D. Lang, and H. Henke, "Modeling, quantification, and reduction of the impact of uncontrolled return currents of vias transiting multilayered packages and boards," *IEEE Trans. Electromagn. Compat.*, vol. 52, no. 2, pp. 421–435, May 2010.
[52] M. Friedrich, M. Leone, and C. Bednarz, "Exact analytical solution for the via-plate capacitance in multiple-layer structures," *IEEE Trans. Electromagn. Compat.*, vol. 54, no. 5, pp. 1097–1104, Oct. 2012.
[53] J. Seo, I. Yoon, J. Jung, J. Ryoo, J. Park, W. Lee, D. Ko, and J. Oh, "Miniaturized dual-band broadside/endfire antenna-in-package for 5G smartphone," *IEEE Trans. Antennas Propag.*, vol. 69, no. 12, pp. 8100–8114, Dec. 2021.
[54] K. Buell, D. Cruickshank, H. Mosallaei, and K. Sarabandi, "Patch antenna over RIS substrate: A novel miniaturized wideband planar antenna design," in *Proc. IEEE Antennas Propag. Soc. Int. Symposium. Digest.*, vol. 4, Jun. 2003, pp. 269–272.
[55] D. M. Pozar, *Microwave Engineering*. Hoboken, NJ, USA: Wiley, 2011.
[56] R. Bayderkhani and H. R. Hassani, "Wideband and low sidelobe slot antenna fed by series-fed printed array," *IEEE Trans. Antennas Propag.*, vol. 58, no. 12, pp. 3898–3904, Dec. 2010.
[57] N. Boskovic, B. Jokanovic, M. Radovanovic, and N. S. Doncov, "Novel *Ku*-band series-fed patch antenna array with enhanced impedance and radiation bandwidth," *IEEE Trans. Antennas Propag.*, vol. 66, no. 12, pp. 7041–7048, Dec. 2018.

HYUNJIN KIM (Member, IEEE) received the B.S. degree in electronic engineering from Korea University, Seoul, South Korea, in 2006, and the M.S. and Ph.D. degrees in electrical engineering from Seoul National University, Seoul, in 2009 and 2021, respectively.

From 2009 to 2020, he was a Staff Engineer at Samsung Electronics, Suwon, South Korea, responsible for research on advanced antenna technologies for communications, advanced network devices, and mmWave antenna systems. From 2021 to 2024, he was a Postdoctoral Research Fellow with the Department of Electrical and Computer Engineering, Institute of New Media and Communications, Seoul National University, Seoul. He is currently a Principal Engineer at LG Electronics, Seoul, responsible for research on antenna technologies for automotive communications. His research interests include D-band antenna design, mmWave array antenna systems, and metasurfaces.

JUNGSUEK OH (Senior Member, IEEE) received the B.S. and M.S. degrees from Seoul National University, South Korea, in 2002 and 2007, respectively, and the Ph.D. degree from the University of Michigan, Ann Arbor, MI, USA, in 2012.

From 2007 to 2008, he was a Hardware Research Engineer with Korea Telecom, Seongnam, South Korea, working on the development of flexible RF devices. In 2012, he joined the Radiation Laboratory, University of Michigan, as a Postdoctoral Research Fellow. From 2013 to 2014, he was a Staff RF Engineer with Samsung Research America, Dallas, TX, USA, working as a Project Leader of the 5G/millimeter-wave antenna system. From 2015 to 2018, he was a Faculty Member with the Department of Electronic Engineering, Inha University, Incheon, South Korea. He is currently an Associate Professor with the School of Electrical and Computer Engineering, Seoul National University. He has published over 50 technical journal articles and conference papers. His research areas include millimeter-wave (mmWave) beam focusing/shaping techniques, antenna miniaturization for integrated systems, and radio propagation modeling for indoor scenarios.

Dr. Oh was a recipient of the 2011 Rackham Predoctoral Fellowship Award from the University of Michigan. He has served as a TPC Member and the Session Chair for IEEE AP-S/USNC-URSI and ISAP. He has served as a Technical Reviewer for IEEE Transactions on Antennas and Propagation and IEEE Antennas and Wireless Propagation Letters.